Orthogonal liquid-jet impingement on wettability-patterned impermeable substrates

Uddalok Sen,[1] Souvick Chatterjee,[1] Julie Crockett,[2] Ranjan Ganguly,[3] Lisha Yu,[4] and Constantine M. Megaridis[1, *]

[1]*Department of Mechanical and Industrial Engineering,*
University of Illinois at Chicago, Chicago, Illinois 60607, USA
[2]*Department of Mechanical Engineering, Brigham Young University, Provo, Utah 84602, USA*
[3]*Department of Power Engineering, Jadavpur University, Kolkata 700098, India*
[4]*Corporate Research and Engineering, Kimberly-Clark Corporation, Neenah, Wisconsin 54956, USA*

Liquid jet impingement on flat, impermeable substrates is important for a multitude of applications, ranging from electronic equipment cooling, to fuel atomization, and erosion of solid surfaces. On a wettable surface, where a sufficient downstream liquid depth can be sustained after axisymmetric impingement, the jet forms a thin film on the substrate up to a radial distance where the film height suddenly increases, forming a hydraulic jump. On a superhydrophobic surface, where a downstream liquid depth is not naturally sustained, the thin film expands and breaks up into droplets, which are subsequently ejected in a random fashion outward, as carried by their radial momentum. In the present work, a facile, scalable, wettability-patterning approach is presented for delaying or even eliminating droplet breakup in the case of jet impingement on horizontal superhydrophobic surfaces. An analytical expression for predicting the hydraulic jump and droplet breakup locations is developed to designate the proper wettability patterns that facilitate alteration and control of the post-impingement liquid behavior. The axisymmetric model is extended to evaluate the radial variation of the competing forces responsible for film breakup, and a design criterion for the effective wettability patterns is proposed.

I. INTRODUCTION

The orthogonal impingement of a liquid jet on a flat, solid substrate is one of the most well-studied fundamental problems in fluid mechanics. The situation is most commonly observed in daily life when a kitchen faucet is opened and the emanating liquid jet hits the sink below. Upon impingement, the liquid undergoes an orthogonal change of direction and spreads as a thin film until the height of the film suddenly increases. This abrupt increase in the film thickness is known as a hydraulic jump [1].

Jet impingement on solid surfaces is important in several application areas, particularly in the high-rate heat transfer community [2]. Jets have been used for cooling metal surfaces [3, 4], turbine blades [2], and electronic equipment [5, 6], annealing and quenching of metals [2], boiling [7, 8], atomization [9], as well as erosion of solid surfaces [10–12]. Apart from impermeable surfaces, jet impingement on permeable surfaces has found use in applications involving heat transfer from metal foams [13, 14], boiling heat transfer [15], drying [16], and in incontinence products [17]. The phenomenon has been recently used to model astrophysical observations as well [18, 19].

The vast practical importance of the problem has resulted in extensive investigations into the fundamentals of the hydrodynamics of orthogonal jet impingement [20–25]. The inviscid solution was proposed more than a century ago by Rayleigh [26], while Watson [27], in his seminal work, laid out the viscous solution. The model incorporated the boundary layer effects and expressed the hydraulic jump radius as a function of the jet velocity, jet diameter, downstream liquid depth, and the liquid properties. Liu and Lienhard [21] pointed out that the classical Watson model fails to predict a circular hydraulic jump for a large downstream depth. They also proposed that surface tension has a stabilizing effect on hydraulic jumps in thin liquid sheets. The Watson model was expanded by Bush and Aristoff [28] to include the effects of surface tension associated with the curvature of the film at the radial location of the hydraulic jump. Such fundamental investigations were extended to analyze the heat transfer aspects of jet impingement as well [29, 30], and several analytical [31], numerical [32, 33], and experimental [34] studies exist in that regard. The effects of other factors, such as the distance of the nozzle from the substrate [35] and the jet diameter [36] were also observed experimentally.

The majority of studies of jet impingement have dealt with water jets striking a hydrophilic surface, with the jet forming a thin liquid film upon impact on the substrate when a downstream liquid depth exists. A hydraulic jump occurs where the momentum of the radially expanding thin film balances with the hydrostatic head due to the downstream depth and the capillary force associated with the curvature of the film at the location of the jump. Recently, a study by Bhagat et al. [37] suggested that gravity does not play a role in the formation of a circular hydraulic jump. However, that theory is only valid during the initiation of a hydraulic jump or for a jump forming on a substrate of infinite dimensions, which, as the authors of that study pointed out, is not a practical configuration. For a circular hydraulic jump on a finite substrate and under steady state conditions, gravity indeed has a significant effect.

Hydraulic jumps in orthogonal liquid jet impact on smooth hydrophilic surfaces are circular, while they can be polygonal on microstructured hydrophilic sufaces [38, 39]. Jet impingement on superhydrophobic surfaces, which are usually fabricated by chemically modifying a micro-nanotextured surface, has a distinctly different outcome due to the increased mobility of the liquid. A downstream depth cannot be maintained on a superhydrophobic surface unless it is forced. Hence, the radially expanding thin film becomes unstable after some distance and breaks up into filaments or droplets [40]. Those droplets do not adhere to the surface; instead, they are rapidly ejected due to their outward momentum, resulting in a significant loss of liquid.

On superhydrophobic surfaces, the liquid is generally in the Wenzel (embedded) state [41] at the point of impingement, while it can attain the Cassie-Baxter state [42] throughout the rest of the thin film [43]. In other words, barring the point of impingement, an air layer is trapped in the micro- and nanoscale cavities of the solid target, thus changing the hydrodynamic [44] and thermal [45] boundary conditions. Hydrodynamically, researchers have accounted for this by introducing an aggregate slip boundary condition [46–49] at the surface, thus accounting for the shear-free boundary condition over the cavities and the no-slip boundary condition on the structures. From a thermal point of view, for metallic substrates, the boundary condition at the liquid-gas interface can be considered adiabatic due to the low thermal conductivity of the gas, while a conventional convection boundary condition exists at the liquid-solid interface [50].

Wettability-patterned surfaces [51–53] feature spatially-distibuted domains of uniform wettability. Some may include superhydrophilic and superhydrophobic spatial domains on a single substrate, suitably shaped to achieve specific tasks, such as high-throughput fluid transport [53], enhanced condensation [54], atmospheric water collection [55], and selective droplet sliding [56]. Recognizing the potential of wettability-patterned surfaces, a handful of studies [57–60] analyzed droplet impact phenomena on such surfaces. However, a vast knowledge gap remains in the domain of orthogonal liquid jet impingement on wettability-patterned surfaces. Koukoravas et al. [61] demonstrated one such configuration, but in a non-axisymmetric situation, and at low flow rates, while Sen et al. [17] performed experiments of jet impingement on wettability-patterned porous, polymeric substrates. The two aforementioned studies are largely

application-oriented and do not shed much light on the fundamental fluid mechanics of the problem. Hence, an attempt has been made in the present work to provide a theoretical basis of jet impingement on wettability-patterned surfaces.

The present work deals with the fundamentals of orthogonal jet impingement on an axisymmetrically wettability-patterned, impermeable, horizontal substrate. An analytical methodology is employed to calculate the hydraulic jump and film breakup radii on a superhydrophobic substrate for a particular jet diameter and impact velocity. The information on these two radii is then used to fabricate spatial domains exhibiting superhydrophobicity and superhydrophilicity, with the goal of altering the post-impingement behavior of the liquid jet, which is demonstrated experimentally. The theoretical model is then implemented to study the radial variation of the forces at the liquid interface, and a design criterion of the wettability pattern is proposed therefrom.

II. MATERIALS AND METHODS

A facile and scalable approach to produce superhydrophobic and superhydrophilic spatial domains on square aluminum samples of dimensions 100 mm × 100 mm (mirror-finish 6061 aluminum sheets, 2 mm thick, McMaster-Carr) was employed; the method (Fig. 1) is the one employed by Koukoravas et al. [61] and Sen et al. [62]. The metal plate samples were initially treated with a 5 M HCl solution (ACS reagent 37%, Sigma-Aldrich) for 4 min (Fig. 1a), followed by passivation in boiling deionized water for 60 min (Fig. 1c). Boiling facilitates the growth of micro-nano structures on the surface of the sample due to the formation of a thin layer of aluminum oxide hydroxide (Al(O)OH) or böhmite [63]. The böhmite layer renders the surface superhydrophilic. Following the work of other researchers [64, 65], the superhydrophilic samples were then immersed in a 1% (by weight) solution of 1H,1H,2H,2H-perfluorodecyltriethoxysilane (97%, Sigma-Aldrich, fluoro-alkyl silane (FAS)) in ethanol (200 proof, Decon Labs) for 8-10 h (Fig. 1e), which created a monolayer of FAS on the roughened Al substrates, thus rendering them superhydrophobic (by reducing the surface energy of the exposed area of the sample). Scanning electron micrographs (obtained using the imaging module of a Raith 100 eLINE electron beam lithography system) at different stages of sample preparation are shown in Figs. 1b, d. Acid-etching produces microscale terraces and caverns (Fig. 1b), which are subsequently covered by nanoscale böhmite needles (Fig. 1d) when passivated in boiling water. Such hierarchical structures (nanoscale strucures formed on top of microscale surface roughness features) are critical for achieving either superhydrophilic or superhydrophobic behavior. The surfaces used in the present work had an average roughness of $\sim 25\mu$m (measured using a Wyko NT3300 optical profilometer). A computer-aided design (CAD) file was fed as vector image to a laser marking system (EMS400, TYKMA Electrox) in order to selectively ablate the FAS coating on the Al samples using a Yb laser (20% power, 20 kHz, 200 mm/s traverse speed, Scorpion Rapide, TYKMA Electrox) (Fig. 1f). The laser ablation exposed the underlying superhydrophilic surface, while the unablated regions remained superhydrophobic. The superhydrophobic regions exhibited a sessile water droplet contact angle of $150 \pm 5°$ (Fig. 1h), whereas a droplet dispensed on the superhydrophilic domain spread instantly with a contact angle below $5°$. Figure 1g presents a schematic top view of the patterned sample obtained from the aforementioned procedure. The salient dimensions of the pattern are its inner (R_i) and outer radii (R_o). The genesis of this particular design will be rationalized in the following section.

Deionized water was used as the probe fluid. A schematic of the experimental setup is shown in Fig. 2. A diaphragm-based storage tank (RO132 4.0 gallon expansion tank, Express Water) fitted with an air compressor (BDINF12C 12V multipurpose inflator, Black & Decker) was used as the fluid delivery system. The storage tank contained both air and water, separated by a rubber diaphragm. Pressurized air from the compressor inflated the diaphragm, which in turn pumped the water out of the tank through a 2 mm inner diameter dispensing syringe (5 mL Luer-Lok Tip, Ref 309646, Becton Dickinson), placed at a vertical distance of 30 mm from the sample. A high-speed digital camera (Phantom Miro 310, Vision Research AMETEK with Nikkor 50 mm lens, Nikon) was used to capture high-speed videos (at 1000 frames-per-second) of the jet impact event, once steady state had been achieved. The videos were further analyzed using ImageJ[66] (open-source image-analysis software distributed by the National Institutes of Health).

III. EXPERIMENTAL RESULTS

Axisymmetric jet impingement experiments were performed for a steady water jet, a typical jet being of 2 mm diameter at 800 mL/min, which corresponds to a jet Reynolds number, Re ($= Q/\pi a\nu$, where Q is the jet flow rate, a the jet radius, and ν the kinematic viscosity of the liquid) $\simeq 4200$, and a Weber number, We ($= \rho Q^2/\pi^2 \sigma a^3$, where ρ is the liquid density, V the speed of the jet, and σ the air-liquid surface tension) $\simeq 250$. As the jet impacts the superhydrophobic substrate, it spreads radially in the form of a narrow film, and then breaks up at its periphery in the form of radially-propagating tiny droplets. The specific flow rate was chosen such that the film breakup occured
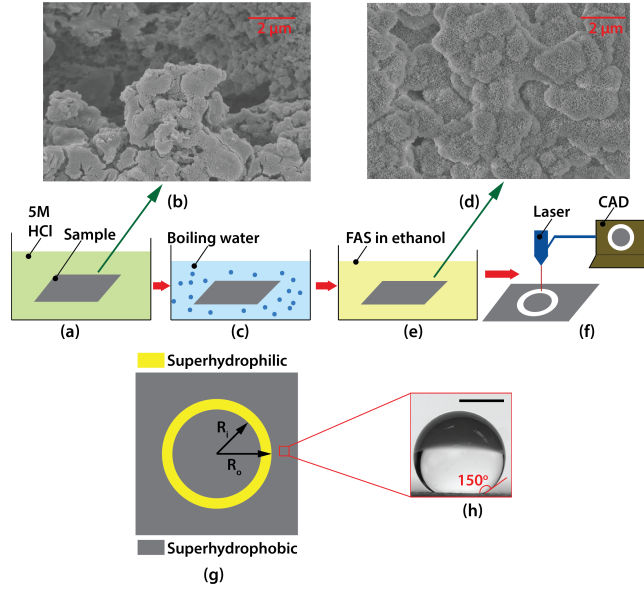
FIG. 1. Schematic of sample preparation procedure: (a) Aluminum plates were immersed in 5 M HCl solution for 4 min; (b) scanning electron micrograph of acid-etched sample; (c) acid-etched samples were passivated in boiling deionized water for 60 min; (d) scanning electron micrograph of etched-and-boiled sample; (e) etched-and-boiled samples were then treated in an ethanolic solution of FAS and kept undisturbed for 8-10 h; (f) CAD-based design was patterned onto the substrate by laser ablation; (g) the final sample containing the superhydrophobic and superhydrophilic domains; and (h) sessile water droplet on the superhydrophobic domain exhibiting a contact angle of $150° \pm 5°$ (scale bar denotes 1 mm).
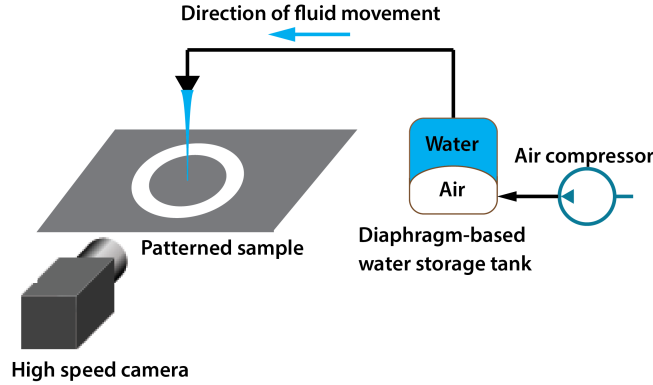

FIG. 2. Schematic of the experimental setup.

at a radial location (from the point of impact) that is within the ends of the square substrate. The design evolution $(A - C)$ for the wettability pattern along with the corresponding experimental snapshots are presented in Fig. 3.

The first sample tested was uniformly superhydrophobic (Fig. 3a1). Figure 3a2 shows an image of the corresponding jet impingement pattern. Post-impingement, the liquid exhibits rapid lateral spreading in the form of a radially-outward thin film, until a radial location where the film abruptly breaks up into droplets. The radial location of this transition, R_b, was measured to be $\simeq 19$ mm. Unlike a circular hydraulic jump, the liquid thin film breaks up into droplets that are ejected randomly from the rim due to their high momentum. This phenomenon has also been observed by other researchers [17, 40] while studying jet impingement on superhydrophobic surfaces.

The first wettability pattern (design B) tested had a circular superhydrophobic region of radius $R = 16$ mm ($R \gg a$, where a is the jet radius), surrounded by a superhydrophilic domain (Fig. 3b1). The two regions met at a circular, sharp wettability contrast line. A snapshot of a steady, impinging jet is shown in Fig. 3b2, which depicts a situation similar to a classical circular hydraulic jump formed at $R_j \simeq 18$ mm from the central point of jet impact. This distance is equal to the calculated jump radius on a ubiquitous superhydrophilic surface with an imposed downstream depth equal to the maximum liquid height that can be sustained on the superhydrophobic domain (the expression for this maximum height is provided in the following section and in section S3 of [67]). This indicates that this specific type
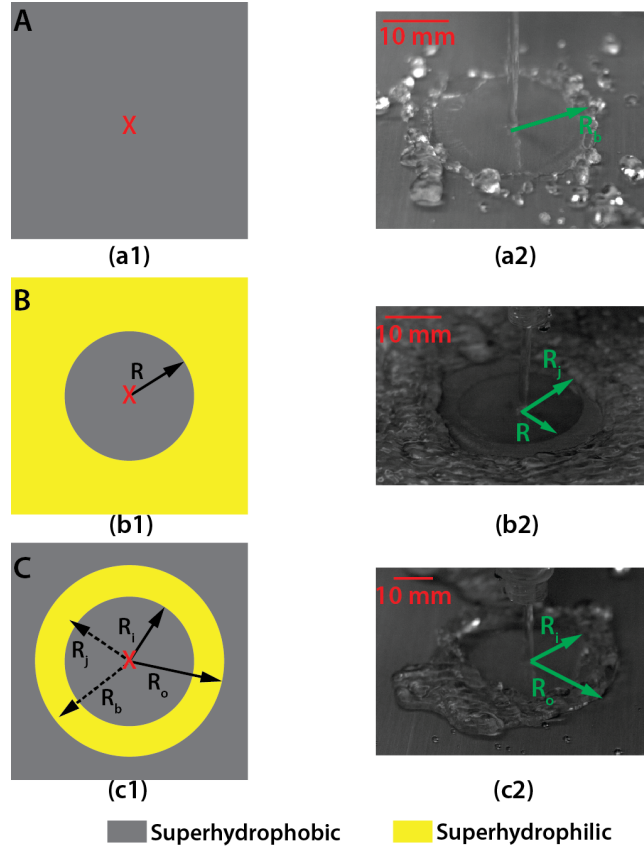
FIG. 3. Evolution of wettability pattern design (A – C) and corresponding experimental snapshots (at 800 mL/min, right column): (a1) design A and (a2) image of jet impingement on a substrate with design A exhibiting film breakup into droplets at breakup radius, $R_b \simeq 19$ mm; (b1) design B and (b2) image of jet impingement on substrate with design B and $R = 16$ mm; circular hydraulic jump forms at jump radius, $R_j \simeq 18$ mm, thus eliminating film breakup into droplets; (c1) design C and (c2) image of jet impingement on substrate with design C, with $R_i = 16$ mm and $R_o = 22$ mm; the film breakup, which occurs at R_o, is more orderly than that shown in Fig. 3a2. The red X marks the spot of orthogonal jet impact on all three wettability patterns. The relative positions of R_b (of Fig. 3a2) and R_j (of Fig. 3b2) have also been marked by dashed arrows in Fig. 3c1.

of wettability patterning (creating a wettability contrast line at a radial location less than the R_j) does not affect the location of the hydraulic jump. However, the droplet break-up seen on the superhydrophobic surface is now absent, being replaced by the post-jump elevated fluid, which persists beyond the radius R_j. Figure 3b2 clearly shows that wettability patterning can alter the post-impingement fluid behavior. It is important to note that, on an intrinsically non-wettable surface, rendering a large area (the outer region, see Fig. 3b1) of the substrate superhydrophilic is an energy-intensive option (e.g., laser ablation in the present case). Hence, a rational design would aim to minimize the area of the superhydrophilic region to achieve control over the radially-spreading thin film. Based on this aim, the next tested design was pattern C (Fig. 3c1), which rendered a narrow superhydrophilic annular region on the otherwise superhydrophobic substrate.

Pattern C (Fig. 3c1) consists of a superhydrophilic annulus (inner radius R_i, outer radius R_o) laid on superhydrophobic surroundings. The annulus contains the R_b and R_j locations of Figs. 3a2 and 3b2, respectively. When a jet impacts the central spot of a design C-patterned sample at a rate of 800 mL/min, as shown in Fig. 3c2, both circular hydraulic jump and subsequent breakup (into droplets) are observed. The spreading thin film forms a hydraulic jump within the superhydrophilic annulus due to the liquid buildup forced by the superhydrophilic domain. The jump location, expectedly, was measured to be the same as R_j of Fig. 3b2. Past the hydraulic jump, the liquid film spreads further until the outer radius R_o of the annulus, where it breaks up into randomly ejected droplets or intermittent streams. The droplets formed in this case are much larger ($\simeq 6$ mm diameter) and slower than the ones observed for an all-superhydrophobic surface ($\simeq 2.5$ mm diameter, Fig. 3a2). As a result, they slowly slide on the surface instead of being rapidly ejected from it. Hence, we have shown that the film breakup location and dynamics upon jet impingement on a superhydrophobic surface can be altered by modifying the wettability of only a small radial portion of the substrate. Snapshots of experiments, similar to that of Fig. 3 but at a higher flow rate (1000 mL/min),

are presented in section S1 of [67], while section S2 of [67] contains snapshots of experiments at 800 mL/min on design C-patterned substrates with different values of R_i and R_o. The experimental outcomes further motivated us to perform a theoretical analysis to explain the mechanics and obtain an engineering design criterion to control the inertia of the droplets formed due to film breakup upon orthogonal impingement of a liquid jet on a superhydrophobic, impermeable substrate. Below, we focus our analysis to identify the limits of R_i and R_o in design C of Fig. 3c1.

IV. THEORETICAL FORMULATION

The goal is to alter the liquid breakup location on an otherwise superhydrophobic substrate by forming a super-hydrophilic annulus centered at the jet impingement location. The wettable annulus should enclose the region where the breakup of the liquid film would otherwise happen, or else the liquid film would break up either upstream (if $R_i > R_b$) or downstream (if $R_o < R_b$) of the annulus. We assume the liquid in the annulus to build up to a height equivalent to the maximum height, H_{max}, occurring for a stationary pool of water on the superhydrophobic surface. This assumption is justified by the fact that the buildup is dependent on the advancing contact angle of the liquid in this domain. The maximum height is defined by a balance between gravity and the air-liquid surface tension

$$\rho g H_{max}^2 = \sigma[1 + \cos(\pi - \phi)] \tag{1}$$

where σ is the air-liquid surface tension, and ϕ the contact angle of a circular advancing liquid front on the superhydrophobic substrate. A detailed derivation is presented in Section S3 of [67].

The analysis and modeling of the radially-expanding thin film on the surface follows the work of Prince et al. [40] closely and is briefly summarized here. We consider a vertical liquid jet of speed V, with a volumetric flow rate Q, kinematic viscosity ν, and radius a impinging on a superhydrophobic horizontal surface, as illustrated in Fig. 4. The jet spreads out in a thin film, and the film thickness decreases as the jet spreads radially outward (as required by mass continuity) until the location of the hydraulic jump. For jet Reynolds number ($Re = Q/\pi a\nu$) smaller than nominally 2.5×10^4, a laminar boundary layer of thickness δ develops from the impingement point and grows with the radial coordinate r. At $r = r_0$, the boundary layer attains the height of the thin film, i.e. $\delta(r) = h(r)$. Following the analysis of Watson [27], we assume that outside of the boundary layer, the velocity remains constant (and is equal to the approaching jet velocity); but for $r > r_0$, the velocity at the air-liquid interface, $U(r)$, decreases with increasing r due to the viscous influence of the wall. For a superhydrophobic plate, an apparent slip velocity that varies with r can exist at $z = 0$, where z is the coordinate normal to the surface. Predicting the slip velocity requires estimation of the slip length at the surface, as discussed in Refs. [40, 46]. A previous study by Joseph et al. [68] suggested that the effective slip length [44], b_{eff}, is related to the lateral length scale between the surface structures, L, through $b_{eff} = \alpha L$, where $\alpha \simeq 0.28$ leads to the best fitting of the experimental results. In the present work, the value of $L \simeq 1$ μm for the randomly microstructured surface (Figs. 1b and 1d) and hence, $b_{eff} = 2.8 \times 10^{-4}$ mm, which when normalized by the jet radius ($a = 1$ mm) leads to a normalized slip length, $\hat{\lambda} = 2.8 \times 10^{-4}$. This falls far short of the $\hat{\lambda} = 0.05$ used by Prince et al. [46], who found that a flow with smaller slip would be indistuingishable from a flow in a zero-slip scenario. Therefore, we assumed zero slip on the solid surface (i.e., at $z = 0$).

To estimate the momentum in the expanding thin film, the analysis is divided into two regions. In region 1 ($r \leq r_0$), the velocity profile is developing and $\delta < h$. In region 2 ($r_0 < r < R_b$ or $r_0 < r < R_j$), the velocity profile is fully-developed (i.e. the boundary layer extends to the height of the film). In both regions 1 and 2, the flow is assumed steady and a control volume formulation of conservation of mass and the linear momentum principle is applied to the jet and spreading thin film. The velocity distributions within the boundary layer in region 1 and the entire thin film in region 2 are assumed to be of the cubic form [46], and invoking the appropriate boundary conditions [46] results in the following expression for the velocity profile

$$u = \frac{3}{2}V\frac{z}{\delta} - \frac{1}{2}V\frac{z^3}{\delta^3} \tag{2}$$

for region 1 and

$$u = \frac{3}{2}U\frac{z}{h} - \frac{1}{2}U\frac{z^3}{h^3} \tag{3}$$

for region 2, where the free surface velocity U varies with r. The radial variation of U can be obtained from mass conservation, which yields
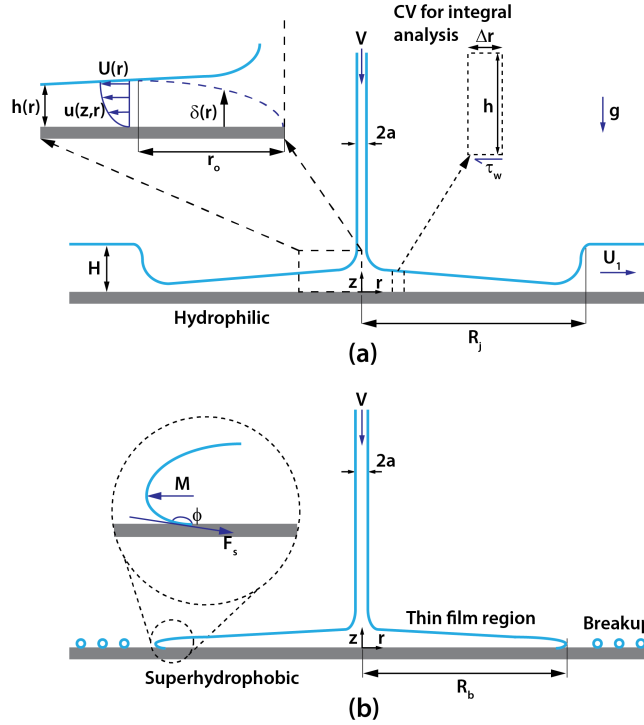
$$U = \frac{4a^2V}{5rh} \tag{4}$$

FIG. 4. Schematic illustrating an axisymmetric, liquid-jet impingement event on: (a) a uniformly-hydrophilic surface, forming a hydraulic jump, and (b) a uniformly-superhydrophobic surface, resulting in film breakup into droplets.

The velocity profiles from Eqs. 2 (for region 1) and 3 (for region 2) are each substituted into the mass and momentum balance equations, and the result is a system of equations for both regions 1 and 2. The solution yields the local liquid radial velocity and thin film height; the local wall shear stress and boundary layer thickness can then be calculated as functions of the jet Reynolds number.

At the radial extent of the thin film, just before breakup, the fluid is advancing and ϕ is greater than $90°$. Accompanying the curved interface is a pressure jump defined by Laplace's equation [69], which depends on R_1 and R_2, the two radii of curvature at the surface. R_1 is the radius of curvature around the thin film, and R_2 is the radius of curvature at the surface. At breakup conditions, $R_1 = R_b$ and $R_b \gg R_2$. Assuming the advancing film front has a uniform radius of curvature, and using geometrical considerations, R_2 can be expressed as a function of the local film height, h, and ϕ. Then the pressure jump across the edge of the spreading thin film front can be expressed as

$$\Delta P = \frac{\sigma}{h}[1 + \cos(\pi - \phi)] \tag{5}$$

A radial momentum balance at the location of breakup is governed by the equilibrium between the momentum flux of the spreading thin film and the pressure jump at its edge. Here, the momentum flux of the droplets leaving the film is neglected, which has been shown to be a good approximation [40]. Substituting ΔP from Eq. 5 and the velocity profile of Eq. 2 (region 1) or Eq. 3 (region 2), and then integrating the momentum flux term gives

$$\sigma[1 + \cos(\pi - \phi)] = \rho V^2(h - \frac{18}{35}\delta) \tag{6}$$

for region 1 and

$$\sigma[1 + \cos(\pi - \phi)] = \rho \frac{17}{35}U^2 h \tag{7}$$

for region 2. The radial breakup location, R_b, is estimated by calculating the right-hand side throughout regions 1 and 2 of the thin film, and when it is balanced by the left-hand side, breakup is expected. We note that the factor $18/35$ or $17/35$ appears due to the integration of u^2 over the height of the boundary layer. A corresponding factor arises in the calculations of Watson [27], where a similarity solution is assumed within the thin film. For region 2, the factor used by Watson [27] is 0.476, whereas the factor for the cubic profile assumed here is 0.486 (2% greater).

This is an unformatted version of the same article that appeared in Phys. Rev. Fluids 4, 014002 (2019).

7

In the present work, the right-hand side of Eq. 7 appears as a function of r, while the left-hand side is constant for a particular surface (constant ϕ) and a particular fluid (specified σ).

An expression to estimate the location of the hydraulic jump on a surface is deduced following the approach of Bush and Aristoff [28]. The integral momentum balance between gravitational and air-liquid surface tension forces, and momentum fluxes into and out of a control volume (inset of Fig. 4a) of vanishing radial width (Δr) at the jump radius, R_j, gives the following expression

$$\frac{1}{2}\rho g(H^2 - h_j^2) + \frac{\sigma(H - h_j)}{R_j} = \rho \int_0^{h_j} u^2 dz - \rho U_1^2 H \tag{8}$$

where H is the downstream water depth, U_1 the downstream water velocity (assumed to be uniform [27]), and h_j the thin-film thickness at the location just prior to the jump ($r = R_j$). Watson [27] neglected the surface tension in his analysis, while Bush and Aristoff [28] showed that it exerts a small, but not negligible, influence on predicting the overall jump location. Thus, the surface tension term has been included here.

Conservation of mass evaluated just downstream of the jump yields

$$Q = 2\pi R_j U_1 H \tag{9}$$

Solving Eq. 9 for U_1 and substituting the result and the velocity profile of Eq. 3 (assuming within region 2) into Eq. 8 gives an equation relating R_j with h_j and U, which are both functions of radial position, as described above. Thus,

$$\frac{35}{17}\left(\frac{g(H^2 - h_j^2)}{2} + \frac{\sigma(H - h_j)}{\rho R_j} + \frac{a^4 V^2}{4R_j^2 H}\right) = U^2 h_j \tag{10}$$

Here, we deviate from prior work and assume the downstream depth H to be the maximum possible height of the jump, H_{max}, that will build up on a superhydrophobic surface purely due to contact angle. This is because the buildup of fluid within the superhydrophilic annulus will be governed by the advancing contact angle of the liquid on the superhydrophobic domain outside the superhydrophilic annulus as the liquid flows from the wettable to the non-wettable area. This maximum height can be calculated from Eq. 1. Using $H = H_{max}$, values of U and h for all r are input into Eq. 10 until it is satisfied, and there the expected jump radius, R_j, is uniquely defined.

For a jet of 800 mL/min impinging on a superhydrophobic surface exhibiting $\phi = 150°$, the value of R_b predicted by this method is 19.12 mm, which closely matches the experimentally-measured value of $\simeq 19$ mm (Fig. 3a2). This indicates that the analytical model with no slip is a reasonably accurate description of the fluid mechanics of the problem. Moreover, the hydraulic jump radius, R_j, calculated by this method for the same jet on the same superhydrophobic surface with $\phi = 150°$ was found to be 18.12 mm if H_{max} (= 5.83 mm for water on a surface with $\phi = 150°$) occurred downstream. This theoretically-predicted value closely matches the measured value of $R_j \simeq 18$ mm in Fig. 3b2. This further suggests that the estimate of H_{max} being the steady-state build up downstream is reasonable, even though this applies for static build up and maximum elevation for a superhydrophobic surface.

For design C in Fig. 3c1, the superhydrophilic annular rim must contain both the hydraulic jump on a wettable surface and the breakup location on a superhydrophobic one. Otherwise, if $R_i > R_b$, the breakup will occur upstream of the annulus (within the superhydrophobic domain, before the fluid reaches the superhydrophilic annulus), or the thin film will completely cover the superhydrophilic annulus if R_j or $R_b > R_o$.

To estimate the velocity of the fluid within the annulus, a local momentum balance is performed. We start with the hydraulic jump equation (Eq. 10), where H_{max} and R_j are imposed. Equation 10 is rearranged and solved for the local post-jump velocity, U_2, within the annulus at radial location R_j. Then

$$U_2 = \left(\frac{17}{35}\frac{h_j U_j^2}{H_{max}} - \frac{g}{2}\frac{H_{max}^2 - h_j^2}{H_{max}} - \frac{\sigma}{\rho}\frac{H_{max} - h_j}{H_{max} R_j}\right)^{1/2} \tag{11}$$

where U_j is the velocity at the top of the film just prior to the jump. Here, the outward momentum is balanced by both the hydrostatic head offered by the downstream rise and the air-liquid surface tension pull at the far edge of the annular rim. Post-jump, the fluid buildup is large enough to engulf the annulus. Hence, it is reasonable to assume that a constant liquid height H_{max} is maintained within the annulus for the radial range $R_j \leq r \leq R_o$. Via mass conservation, the radial liquid-front velocity U_3 at any r in the range (R_j, R_o) is
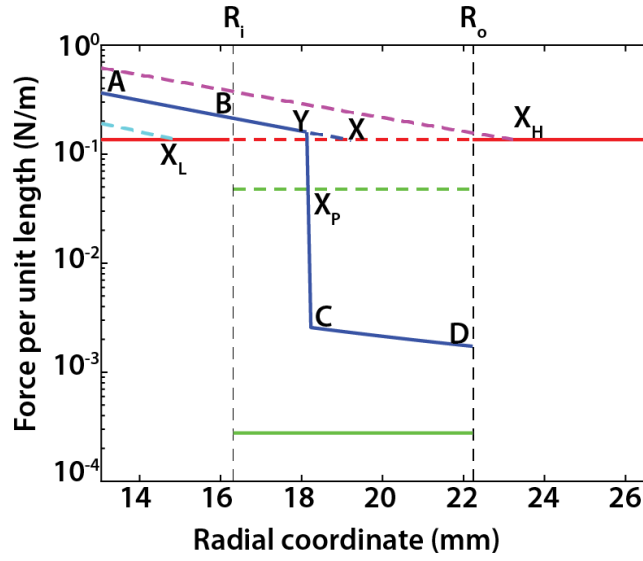
$$U_3(r) = \frac{R_j}{r}U_2 \tag{12}$$

FIG. 5. Radial variation (in the vicinity of the annulus with $R_i = 16$ mm and $R_o = 22$ mm) of driving momentum ($\rho\frac{17}{35}U^2h$) and resistive capillary forces ($\sigma[1 + \cos(\pi - \phi)]$) per unit length at the curved advancing film front for a jet flow rate of 800 mL/min. The blue dashed line (ABX) represents the radial variation of momentum force per unit length for a completely superhydrophobic surface, while the blue solid line (ABYCD) represents the radial variation of momentum force per unit length when the superhydrophilic annulus is present. The red line (both solid and dashed parts) denotes the maximum value of the resistive capillary force per unit length on the superhydrophobic domain (calculated for $\phi = 150°$), while the green solid line denotes the same on the superhydrophilic domain ($\phi = 5°$). X denotes the radial location where the momentum and capillary forces balance, indicating the onset of film breakup on a superhydrophobic surface; Y denotes the location of the hydraulic jump on a superhydrophobic surface with a superhydrophilic annulus. The dashed magenta line (running parallel to the line ABYX) represents the radial variation of the momentum force for a flow rate of 1000 mL/min; film breakup is observed at X_H ($\simeq 23$ mm), which exceeds R_o. The dashed cyan line, on the other hand, shows the radial variation of momentum for a 600 mL/min jet, and the point X_L ($\simeq 15$ mm) denotes the location of film breakup for that flow rate on the superhydrophobic surface; X_L is radially located inside R_i. The dashed green line represents the capillary force on a slightly hydrophilic surface ($\phi = 70°$); the point X_P (at radial distance less than R_o) denotes where breakup would be observed for a similar annulus with $\phi = 70°$ and a jet flow rate of 800 mL/min.

V. ANALYSIS AND DESIGN RAMIFICATIONS

The present section considers the annular wettability pattern (design C of Fig. 3c1) and is aimed at recognizing how the hydraulic jump and breakup locations will vary depending on the variation of the jet momentum, the geometry of the annular region, and the wettability contrast between the wettable and the non-wettable domains. The radial location of film breakup is governed by the balance between the force due to the momentum of the radially expanding liquid film ($\rho\frac{17}{35}U^2h$), which is driving the process, and the resistive capillary force ($\sigma[1 + \cos(\pi - \phi)]$) associated with the curvature of the liquid periphery. The balance is expressed mathematically in Eq. 7. This balance is disrupted by the presence of the narrow superhydrophilic annulus. The radial variation of the momentum and capillary forces is shown in Fig. 5 in the vicinity of the superhydrophilic annulus for the 2 mm diameter jet impacting orthogonally on the design C-patterned substrate (Fig. 3c1) having $R_i = 16$ mm and $R_o = 22$ mm. The red line in Fig. 5 represents the maximum value of the resistive capillary force which is dependent on ϕ ($= 150°$ in this case) only, hence it remains constant with radial spread. The blue line (solid along ABY and then dashed along YX) represents the radial variation of the momentum force (right-hand side of Eq. 6 for region 1 and of Eq. 7 for region 2) on an entirely superhydrophobic surface (Fig. 3a2) for a flow rate of 800 mL/min. The intersection of the blue and red lines, i.e., point X in Fig. 5, marks the radial location where the momentum and capillary forces balance one another, and it is where the film would breakup into droplets on a purely superhydrophobic surface.

When the jet impinges on a design C-patterned substrate with $R_i = 16$ mm and $R_o = 22$ mm, the radial variation of the momentum force initially follows the solid blue line AB. At point B, the liquid encounters the superhydrophilic annulus. It is important to note that the wettability contrast line remains immersed in the fluid, and the surface textures in the superhydrophobic and superhydrophilic regions do not differ much (see discussions in Section III). Therefore, the liquid film momentum force keeps declining with the same law along BY even beyond the wettability contrast line at R_i. This also implies that the hydraulic jump radius should be insensitive to the presence of the

wettability contrast line. This corroborates to our experimental observation (see Fig. 3) where the R_j on a completely superhydrophobic surface closely matched that on the design C-patterned surface. The momentum of the spreading film suddenly changes at radius R_j (point Y) – the velocity of the liquid abruptly decreases, due to the presence of the hydraulic jump with a post-jump height H_{max}. As already mentioned in Section IV (and Section S3 of [67]), H_{max} is governed by the advancing contact angle on the domain outside the superhydrophilic annulus. Therefore, the momentum force per unit length at $r > R_j$ can be expressed as $\rho U_3^2 H_{max}$, where U_3 is governed by Eq. 12. The radial variation of $\rho U_3^2 H_{max}$ is shown in Fig. 5 by the line CD. One may notice that the line CD is well below the red line associated with the maximum capillary force on a superhydrophobic surface. However, liquid breakup is not observed in the experiments (Fig. 3c2). This is because the maximum capillary force within the superhydrophilic annulus does not follow the red dashed line. The value of the advancing contact angle, ϕ, is much lower in the superhydrophilic annulus. Hence, the left hand side of Eq. 7 has a much lower value (~ 500 times smaller compared to that for the superhydrophobic surface), and is represented by the solid green line of Fig. 5 within the annulus. The above numerical value was computed by assuming $\phi = 5°$, since it was difficult to measure the exact advancing contact angle on the superhydrophilic surface. Hence, within the superhydrophilic annulus, the momentum force of the fluid still remains greater than the resistive capillary force, and film breakup cannot occur. Note, however, that film breakup would have been observed within the annulus if the capillary force were larger; having a hydrophilic annulus (instead of superhydrophilic) of larger ϕ would lead to the capillary force line (solid green) intersect the blue line at a radial location upstream of R_o. One such instance is shown in Fig. 5, where the contact angle on the hydrophilic annulus is taken as $70°$; the corresponding capillary force is represented by the green dashed line in this case. The solid blue line (representing the momentum variation) intersects the green dashed line (denoting the capillary force) at point X_P, thus indicating that film breakup would have been observed inside the annular wettable domain itself (i.e., at a radial location $< R_o$). In other words, if the breakup needs to be kept at bay over the wettable annulus, the maximum allowable value of R_o will be determined by the radial location of X_P. Clearly, this criterion puts a limit on the choice of R_o and, subsequently, the radial width of the hydrophilic annulus itself.

When the spreading film crosses the wettable annulus and enters the outer superhydrophobic domain at $r = R_o$, the momentum force exerted by the spreading liquid front (point D in Fig. 5) falls short of the maximum resistive capillary force (denoted by the solid red line again, since the liquid is now spreading on the superhydrophobic domain). Hence, the liquid film breaks up at R_o. The film breakups at location X (for an entirely superhydrophobic surface) or at location D (for a superhydrophobic surface with a superhydrophilic annulus) take place at two distinctly different levels of liquid film momentum. The momentum of the liquid at point X (superhydrophobic surface) is much higher than that at point D (superhydrophilic annulus on superhydrophobic surface). As reported in the literature [70], the higher the momentum of the liquid sheet prior to breakup, the smaller are the droplets. This is corroborated by the experimentally-observed behaviors of the post-breakup regions in Figs. 3a2 and 3c2. It is evident from the experimental images that smaller and faster droplets are produced on a completely superhydrophobic surface; some of these droplets fly off the surface outward from the breakup location (X of Fig. 5). On the other hand, the droplets produced at the outer boundary, D, of the superhydrophilic annulus are larger and glide slower on the surface. Figure 5 was drawn for a 800 mL/min jet, but a similar figure can be produced for any commensurate flow rate in the laminar regime.

The respective bounds of R_i ($R_i \leq R_j$) and R_o ($R_o \geq R_b$) are, expectedly, dependent on the jet flow rate, since R_b and R_j also depend on the flow rate. Two such instances with different flow rates have been demonstrated in Fig. 5 by the dashed cyan and magenta lines. The dashed cyan line represents the radial variation of momentum force (per unit length) for a jet flow rate of 600 mL/min, which intersects the capillary force line (solid red) corresponding to the superhydrophobic domain at point X_L (at radial location $< R_i$), thus indicating that the spreading film would break up before reaching the superhydrophilic annulus. However, for a jet flow rate of 1000 mL/min (dashed magenta line), film breakup is marked by the point X_H, at a radial location $> R_o$. Hence, the superhydrophilic annulus with $R_i = 16$ mm and $R_o = 22$ mm does not influence the film breakup behavior for this higher flow rate. The experimental snapshots for the jet flow rates of 600 mL/min and 1000 mL/min, which are shown in Section S4 of [67], confirm the outcome predicted in Fig. 5.

For any given flow rate, the limiting values of the dimensions of the superhydrophilic annulus of pattern C (Fig. 3c1) are determined by the hydraulic jump and film breakup radii on the non-wettable domain for the same flow rate. Mathematically, $R_i \leq R_j$ and $R_o \geq R_b$. Hence, the minimum width of the annulus can be expressed as $(R_b - R_j)$, while the maximum radial location where the superhydrophilic domain can start is R_j. A ratio of these two quantities, $(R_b - R_j)/R_j$, effectively represents the limiting design dimensions of the superhydrophilic domain for a particular flow rate and repellency of the non-wettable domain. Both R_b and R_j are dependent on the fluid momentum force and the capillary force on the non-wettable domain, as observed from Eqs. 1, 7, and 10. The breakup radius, R_b, is dependent on the dynamic interplay between the fluid momentum and air-liquid surface tension, hence it is a function of the jet Weber number, We ($= \rho Q^2/\pi^2 \sigma a^3$). The hydraulic jump radius, R_j, is dependent on the maximum fluid height, H_{max}, that can be sustained on the non-wettable domain, which, in turn, depends on the contact angle ϕ.
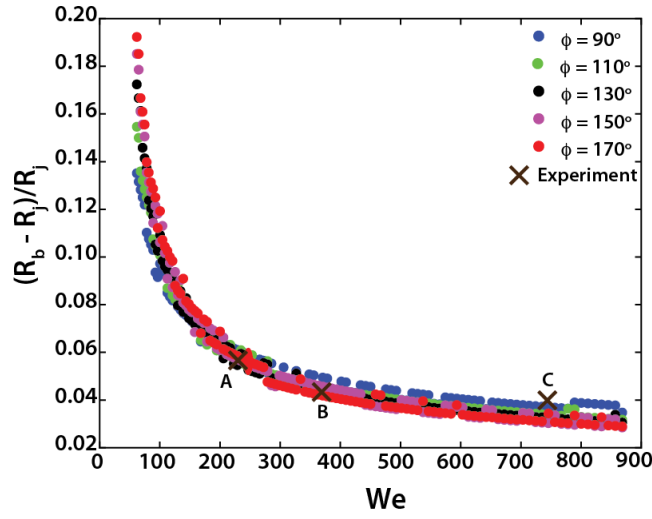
FIG. 6. Variation of $(R_b - R_j)/R_j$ with We for five different values of ϕ ranging from $90°$ to $170°$; ϕ represents the contact angle on the non-wettable domain. The quantity along the abscissa (We) represents the jet flow rate, while that on the ordinate scales the limiting dimensions of the superhydrophilic annulus of pattern C (Fig. 3c1). The conditions for the experimentally observed data points are: (A) $Q = 800$ mL/min, $a = 1$ mm, $\phi = 150°$; (B) $Q = 1000$ mL/min, $a = 1$ mm, $\phi = 150°$; (C) $Q = 1200$ mL/min, $a = 0.9$ mm, $\phi = 150°$. All the points lie along a single curve, which can facilitate design decisions for any jet flow rate-contact angle combination.

The variation of $(R_b - R_j)/R_j$ with We is shown in Fig. 6 for five different values of ϕ ranging from $90°$ to $170°$. The datapoints in Fig. 6 have been obtained from the theoretical model described in the preceding section. The points marked with an 'X' in Fig. 6 were obtained from experiments (A: $Q = 800$ mL/min, $a = 1$mm, $\phi = 150°$; B: $Q = 1000$ mL/min, $a = 1$ mm, $\phi = 150°$; C: $Q = 1200$ mL/min, $a = 0.9$ mm, $\phi = 150°$) performed by varying both the jet diameter and the jet flow rate. All the points collapse on a single curve, which can be used for design decisions. A fit to the points shown in Fig. 6 yields $(R_b - R_j)/R_j = 1.47We^{-0.58}$ with a coefficient of determination $R^2 = 0.96$. In other words, knowing the liquid jet (We) and the surface wettability (ϕ), one can estimate the limiting dimensions of the superhydrophilic annulus of pattern C (Fig. 3c1) from Fig. 6, as needed to contain a jump and breakup at specified locations. It is known from the literature [28, 40], that both R_j and R_b increase with increasing jet momentum (hence We). This is confirmed by the present theoretical model, as shown in Fig. S5 of [67]. However, the increase of R_j with We is steeper at lower We ($We < 150$) than at higher values. Below this We, breakup was suppressed in the experiments due to the lack of sufficient momentum, a phenomenon reported by others [43] as well. Regarding the linear decrease for $We > 150$, we note that the pressure force in Eq. 7 is a constant, whereas the thin film momentum is a function of We. In addition, from Eq. 10, the respective gravity force, capillary force, and downstream film momentum balance with the thin film momentum, which scales with Re. Yet the forces on the left are functions of R_j. Specifically, the second (capillary force) and third (downstream momentum) terms vary with R_j as $1/R_j$ and $1/R_j^2$, respectively. At low We, or low R_j, the capillary term is of the same order as the gravitational term (dominant term), whereas the downstream momentum term is an order of magnitude smaller, as seen in Fig. S6 of [67], which plots the variations of the capillary, gravity, and downstream depth terms with We. As We increases, the capillary force drops sharply due to the larger thin film radius, and by $We \simeq 150$ - 200, it has begun to level off at a value one order of magnitude lower than the gravitational balancing force. For larger We, R_j and R_b increase at a similar rate as their balancing forces are nearly constant; thus the plot (Fig. 6) decreases at a constant rate. This can also be seen in Fig. S5 of [67].

VI. CONCLUSIONS

The present work demonstrates the use of wettability patterning to impose a 'hydraulic jump' and manipulate the film breakup location on an otherwise superhydrophobic impermeable substrate under axisymmetric, liquid-jet impingement conditions. A facile and scalable approach to selectively alter the spatial wettability of the top surface of an aluminum substrate was employed. A high-momentum water jet ($Re \simeq 4200$) impinging orthogonally on a superhydrophobic substrate results in the radially expanding liquid film to breakup into droplets, while a classical circular hydraulic jump is formed on a superhydrophilic substrate. A synergistic design using these two extreme

wettabilites was sought in order to achieve the desired goal of reining in randomly ejecting droplets.

In the first design tested, the liquid jet impinged on a superhydrophobic circular patch surrounded by a superhydrophilic domain. Film breakup was arrested completely and a circular hydraulic jump was formed at the same radial location as that on an unpatterned superhydrophobic substrate. When the jet hits a superhydrophobic spot that is surrounded by a superhydrophilic annulus, which in turn is surrounded by a superhydrophobic domain, both hydraulic jump and film breakup were observed. Moreover, by suitably designing the annulus (inner and outer radii), the radial location of the film breakup could be shifted further outward than the one on a ubiquitously superhydrophobic substrate. Additionally, on a superhydrophobic substrate, the droplets formed after film breakup are smaller, faster, and tend to fly off the surface instead of gliding on it; whereas on a superhydrophobic substrate with a superhydrophilic annulus, the droplets formed past the annulus are larger, slower, and glide on the surface. In summary, wettability patterning in the present configuration cannot alter the radial location of the hydraulic jump, but can delay the film breakup.

In addition to the experiments, an analytical model was used to predict the radial locations of hydraulic jump and film breakup by balancing the driving momentum force and the resistive capillary force at the curved periphery of the radially expanding liquid film. The hydraulic jump and film breakup locations predicted from the model matched the experimental measurements. The model was then further leveraged to study how the liquid momentum force varies with radial location; this subsequently led to the identification of the limits of the salient dimensions of the superhydrophilic annulus for a range of jet flow rate and surface-wettability conditions.

The present work offers the first analytical-experimental study of high-momentum jet impingement on wettability-patterned substrates. The analytical model provides insight into the fluid mechanics of the problem, and presents the design principles for the wettability patterning approach. The model was validated by experimental results. Although the model used in the present study is not new, the novelty of the work lies in the modification of that model to study jet impingement on wettability-patterned substrates. The present work also studies the radial variation of momentum and capillary forces in such a scenario, and proposes a design criterion for the patterning of such surfaces so as to render control over the liquid film breakup radius – endeavors that have not yet been undertaken in the literature. The findings of this study can be used to facilitate design decisions for a multitude of applications involving orthogonal jet impingement on horizontal substrates.

ACKNOWLEDGEMENTS

[1] F. J. Higuera, "The circular hydraulic jump," Phys. Fluids **9**, 1476–1478 (1997).
[2] A. M. Kuraan, S. I. Moldovan, and K. Choo, "Heat transfer and hydrodynamics of free water jet impinging at low nozzle-to-plate spacings," Int. J. Heat Mass Transfer **108**, 2211–2216 (2017).
[3] K. Jambunathan, E. Lai, M. A. Moss, and B. L. Button, "A review of heat transfer data for circular jet impingement," Int. J. Heat Fluid Fl. **13**, 106–115 (1992).
[4] M. Hadžiabdić and K. Hanjalić, "Vortical structure and heat transfer in a round impinging jet," J. Fluid Mech. **596**, 221–260 (2008).
[5] B. Elison and B. W. Webb, "Local heat transfer to impinging liquid jets in the initially laminar, transitional, and turbulent regimes," Int. J. Heat Mass Transfer **37**, 1207–1216 (1994).
[6] X. Liu, J. H. Lienhard V, and J. S. Lombara, "Convective heat transfer by impingement of circular liquid jets," J. Heat Transfer **113**, 571–582 (1991).
[7] D. H. Wolf, F. P. Incropera, and R. Viskanta, "Local jet impingement boiling heat transfer," Int. J. Heat Mass Transfer **39**, 1395–1406 (1996).
[8] Z.-H. Liu and J. Wang, "Study on film boiling heat transfer for water jet impinging on high temperature flate plate," Int. J. Heat Mass Transfer **44**, 2475–2481 (2001).
[9] J. Mikielewicz and D. Mikielewicz, "A simple dissipation model of circular hydraulic jump," Int. J. Heat Mass Transfer **52**, 17–21 (2009).

[10] A. Kibar, H. Karabay, K. S. Yiğit, I. O. Ucar, and H. Y. Erbil, "Experimental investigation of inclined liquid water jet flow onto vertically located superhydrophobic surfaces," Exp. Fluids **49**, 1135–1145 (2010).

[11] I. S. Bayer, A. J. Davis, E. Loth, and A. Steele, "Water jet resistant superhydrophobic carbonaceous films by flame synthesis and tribocharging," Mater. Today Commun. **3**, 57–68 (2015).

[12] G. Li, M. Liu, J. Wang, D. Chong, and J. Yan, "Numerical study of erosion behavior of rpv lower head wall impinged by molten corium jet with particle method," Int. J. Heat Mass Transfer **104**, 1060–1068 (2017).

[13] T.-M. Jeng and S.-C. Tzeng, "Numerical study of confined slot jet impinging on porous metallic foam heat sink," Int. J. Heat Mass Transfer **48**, 4685–4694 (2005).

[14] K.-C. Wong, "Thermal analysis of a metal foam subject to jet impingement," Int. Commun. Heat Mass Transfer **39**, 960–965 (2012).

[15] Z. Zhao, Y. Peles, and M. K. Jensen, "Water jet impingement boiling from structured-porous surfaces," Int. J. Heat Mass Transfer **63**, 445–453 (2013).

[16] N. D. Francis and W. J. Wepfer, "Jet impingement drying of a moist porous solid," Int. J. Heat Mass Tranfer **39**, 1911–1923 (1996).

[17] U. Sen, S. Chatterjee, P. Sinha Mahapatra, R. Ganguly, R. Dodge, L. Yu, and C. M. Megaridis, "Surface-wettability patterning for distributing high-momentum water jets on porous polymeric substrates," ACS Appl. Mater. Interfaces **10**, 5038–5049 (2018).

[18] G. Jannes, R. Piquet, P. Maïssa, C. Mathis, and G. Rousseaux, "Experimental demonstration of the supersonic-subsonic bifurcation in the circular jump: a hydrodynamic white hole," Phys. Rev. E **83**, 056312 (2011).

[19] J. K. Bhattacharjee, "Tunneling of the blocked wave in a circular hydraulic jump," Phys. Lett. A **381**, 733–736 (2017).

[20] A. D. D. Craik, R. C. Latham, M. J. Fawkes, and P. W. F. Gribbon, "The circular hydraulic jump," J. Fluid Mech. **112**, 347–362 (1981).

[21] X. Liu and J. H. Lienhard V, "The hydraulic jump in circular jet impingement and in other thin liquid films," Exp. Fluids **15**, 108–116 (1993).

[22] T. Bohr, P. Dimon, and V. Putkaradze, "Shallow-water approach to the circular hydraulic jump," J. Fluid Mech. **254**, 635–648 (1993).

[23] N. Rojas, M. Argentina, and E. Tirapegui, "A progressive correction to the circular hydraulic jump scaling," Phys. Fluids **25**, 042105 (2013).

[24] A. Duchesne, L. Lebon, and L. Limat, "Constant Froude number in a circular hydraulic jump and its implication on the jump radius selection," Eur. Phys. Lett. **107**, 54002 (2014).

[25] B. Mohajer and R. Li, "Circular hydraulic jump on finite surfaces with capillary limit," Phys. Fluids **27**, 117102 (2015).

[26] Lord Rayleigh, "On the theory of long waves and bores," Proc. R. Soc. Lond. A **90**, 324–328 (1914).

[27] E. J. Watson, "The radial spread of a liquid jet over a horizontal plane," J. Fluid Mech. **20**, 481–499 (1964).

[28] J. W. M. Bush and J. M. Aristoff, "The influence of surface tension on the circular hydraulic jump," J. Fluid Mech. **489**, 229–238 (2003).

[29] B. W. Webb and C.-F. Ma, "Single-phase liquid jet impingement heat transfer," Adv. Heat Transfer **26**, 105–217 (1995).

[30] D. J. Womac, S. Ramadhyani, and F. P. Incropera, "Correlating equations for impingement cooling of small heat sources with single circular liquid jets," J. Heat Transfer **115**, 106–115 (1993).

[31] Z. H. Chaudhury, "Heat transfer in a radial liquid jet," J. Fluid Mech **20**, 501–511 (1964).

[32] J.-J. Shu and G. Wilks, "Heat transfer in the flow of a cold, two-dimensional vertical liquid jet against a hot, horizontal plate," Int. J. Heat Mass Transfer **39**, 3367–3379 (1996).

[33] J. Sung, H. G. Choi, and J. Y. Yoo, "Finite element simulation of thin liquid film flow and heat transfer including a hydraulic jump," Int. J. Numer. Meth. Eng. **46**, 83–101 (1999).

[34] J. Stevens and B. W. Webb, "Local heat transfer coefficients under an axisymmetric, single-phase liquid jet," J. Heat Transfer **113**, 71–78 (1991).

[35] K. Choo and S. J. Kim, "The influence of nozzle diameter on the circular hydraulic jump of liquid jet impingement," Exp. Therm. Fluid Sci. **72**, 12–17 (2016).

[36] K. Choo, B. K. Friedrich, A. W. Glaspell, and K. A. Schilling, "The influence of nozzle-to-plate spacing on heat transfer and fluid flow of submerged jet impingement," Int. J. Heat Mass Transfer **97**, 66–69 (2016).

[37] R. K. Bhagat, N. K. Jha, P. F. Linden, and D. I. Wilson, "On the origin of the circular hydraulic jump in a thin liquid film," J. Fluid Mech. **851**, R5 (2018).

[38] E. Dressaire, L. Courbin, J. Crest, and H. A. Stone, "Thin-film fluid flows over microdecorated surfaces: observation of polygonal hydraulic jumps," Phys. Rev. Lett. **102**, 194503 (2009).

[39] E. Dressaire, L. Courbin, J. Crest, and H. A. Stone, "Inertia dominated thin-film flows over microdecorated surfaces," Phys. Fluids **22**, 073602 (2010).

[40] J. F. Prince, D. Maynes, and J. Crockett, "On jet impingement and thin film breakup on a horizontal superhydrophobic surface," Phys. Fluids **27**, 112108 (2015).

[41] R. N. Wenzel, "Resistance of solid surfaces to wetting by water," Ind. Eng. Chem. **28**, 988–994 (1936).

[42] A. B. D. Cassie and S. Baxter, "Wettability of porous surfaces," Trans. Faraday Soc. **40**, 546–551 (1944).

[43] D. Maynes, M. Johnson, and B. W. Webb, "Free-surface liquid jet impingement on rib patterned superhydrophobic surfaces," Phys. Fluids **23**, 052104 (2011).

[44] E. Lauga and H. A. Stone, "Effective slip in pressure-driven Stokes flow," J. Fluid Mech. **489**, 55–77 (2003).

[45] R. Enright, N. Miljkovic, A. Al-Obeidi, C. V. Thompson, and E. N. Wang, "Condensation on superhydrophobic surfaces: the role of local energy barriers and structure length scale," Langmuir **28**, 14424–14432 (2012).

[46] J. F. Prince, D. Maynes, and J. Crockett, "Analysis of laminar jet impingement and hydraulic jump on a horizontal surface with slip," Phys. Fluids **24**, 102103 (2012).

[47] M. Johnson, D. Maynes, and J. Crockett, "Experimental characterization of hydraulic jump caused by jet impingement on micro-patterned surfaces exhibiting ribs and cavities," Exp. Therm. Fluid Sci **58**, 216–223 (2014).

[48] J. F. Prince, D. Maynes, and J. Crockett, "Jet impingement and the hydraulic jump on horizontal surfaces with anisotropic slip," Phys. Fluids **26**, 042104 (2014).

[49] R. E. Khayat, "Impinging planar jet flow on a horizontal surface with slip," J. Fluid Mech. **808**, 258–289 (2016).

[50] M. Searle, D. Maynes, and J. Crockett, "Thermal transport due to liquid jet impingement on superhydrophobic surfaces with isotropic slip," Int. J. Heat Mass Transfer **110**, 680–691 (2017).

[51] G. P. López, H. A. Biebuyck, C. D. Frisbie, and G. M. Whitesides, "Imaging of features on surfaces by condensation figures," Science **260**, 647–649 (1993).

[52] D. Qin, Y. Xia, B. Xu, H. Yang, C. Zhu, and G. M. Whitesides, "Fabrication of ordered two-dimensional arrays of micro- and nanoparticles using patterned self-assembled monolayers as templates," Adv. Mater. **11**, 1433–1437 (1999).

[53] A. Ghosh, R. Ganguly, T. M. Schutzius, and C. M. Megaridis, "Wettability patterning for high-rate, pumpless fluid transport on open, non-planar microfluidic platforms," Lab Chip **14**, 1538–1550 (2014).

[54] A. Ghosh, S. Beaini, B. J. Zhang, R. Ganguly, and C. M. Megaridis, "Enhancing dropwise condensation through bioinspired wettability patterning," Langmuir **30**, 13103–13115 (2014).

[55] H. Bai, L. Wang, J. Ju, R. Sun, Y. Zheng, and L. Jiang, "Efficient water collection on integrative bioinspired surfaces with star-shaped wettability patterns," Adv. Mater. **26**, 5025–5030 (2014).

[56] M. Elsharkawy, T. M. Schutzius, and C. M. Megaridis, "Inkjet patterned superhydrophobic paper for open-air surface microfluidic devices," Lab Chip **14**, 1168–1175 (2014).

[57] U. Mock, T. Michel, C. Tropea, I. Roisman, and J. Rühe, "Drop impact on chemically structured arrays," J. Phys.: Condens. Matter **17**, S595–S605 (2005).

[58] T. Michel, U. Mock, I. V. Roisman, J. Rühe, and C. Tropea, "The hydrodynamics of drop impact onto chemically structured surfaces," J. Phys.: Condens. Matter **17**, S607–S622 (2005).

[59] S. Kim, M.-W. Moon, and H.-Y. Kim, "Drop impact on super-wettability-contrast annular patterns," J. Fluid Mech. **730**, 328–342 (2013).

[60] T. M. Schutzius, G. Graeber, M. Elsharkway, J. Oreluk, and C. M. Megaridis, "Morphing and vectoring impacting droplets by means of wettability-engineered surfaces," Sci. Rep. **4**, 7029 (2014).

[61] T. P. Koukoravas, A. Ghosh, P. Sinha Mahapatra, R. Ganguly, and C. M. Megaridis, "Spatially-selective cooling by liquid jet impinging orthogonally on a wettability-patterned surface," Int. J. Heat Mass Transfer **95**, 142–152 (2016).

[62] U. Sen, S. Chatterjee, R. Ganguly, R. Dodge, L. Yu, and C. M. Megaridis, "Scaling laws in directional spreading of droplets on wettability-confined diverging tracks," Langmuir **34**, 1899–1907 (2018).

[63] W. Vedder and D. A. Vermilyea, "Aluminum + water reaction," Trans. Faraday Soc. **65**, 561–584 (1969).

[64] Z. Yu, Y. Yu, Y. Li, S. Song, S. Huo, and X. Han, "Preparation and characterization of super-hydrophobic surfaces on aluminum and stainless steel substrates," Surf. Rev. Lett. **17**, 375–381 (2010).

[65] J. Yang, Z. Zhang, X. Xu, X. Men, X. Zhu, and X. Zhou, "Superoleophobic textured aluminum surfaces," New J. Chem. **35**, 2422–2426 (2011).

[66] C. A. Schneider, W. S. Rasband, and K. W. Elicieri, "NIH Image to ImageJ: 25 years of image analysis," Nat. Meth. **9**, 671–675 (2012).

[67] "See Supplemental Material at (URL will be inserted by publisher) for snapshots of experiments at different flow rates; snapshots of experiments on patterns with different dimensions; the derivation of mathematical expression for liquid height on a superhydrophobic surface; experimental snapshots of jet impingement events, at 600 ml/min and 1000 ml/min, on a design C-patterned substrate; variations of R_b and R_j with We; variations of capillary, gravity, and downstream depth terms with We; non-dimensional forms of the governing equations.".

[68] P. Joseph, C. Cottin-Bizonne, J. M. Benoît, C. Ybert, C. Journet, P. Tabeling, and L. Bocquet, "Slippage of water past superhydrophobic carbon nanotube forests in microchannels," Phys. Rev. Lett. **97**, 156104 (2006).

[69] P.-G. de Gennes, F. Brochard-Wyart, and D. Quéré, *Capillarity and Wetting Phenomena: Drops, Bubbles, Pearls, Waves* (Springer-Verlag New York Inc., 2004).

[70] A. Lozano, F. Barreras, G. Hauke, and C. Dopazo, "Longitudinal instabilities in an air-blasted liquid sheet," J. Fluid Mech. **437**, 143–173 (2001).

SUPPLEMENTAL MATERIAL

Orthogonal liquid-jet impingement on wettability-patterned impermeable substrates

Uddalok Sen[1], Souvick Chatterjee[1], Julie Crockett[2], Ranjan Ganguly[3], Lisha Yu[4], and Constantine M. Megaridis[1,*]

[1]Department of Mechanical and Industrial Engineering, University of Illinois at Chicago, Chicago, IL 60607, USA

[2]Department of Mechanical Engineering, Brigham Young University, Provo, UT 84602, USA

[3]Department of Power Engineering, Jadavpur University, Kolkata 700098, India

[4]Corporate Research and Engineering, Kimberly-Clark Corporation, Neenah, WI 54956, USA

* E-mail: cmm@uic.edu
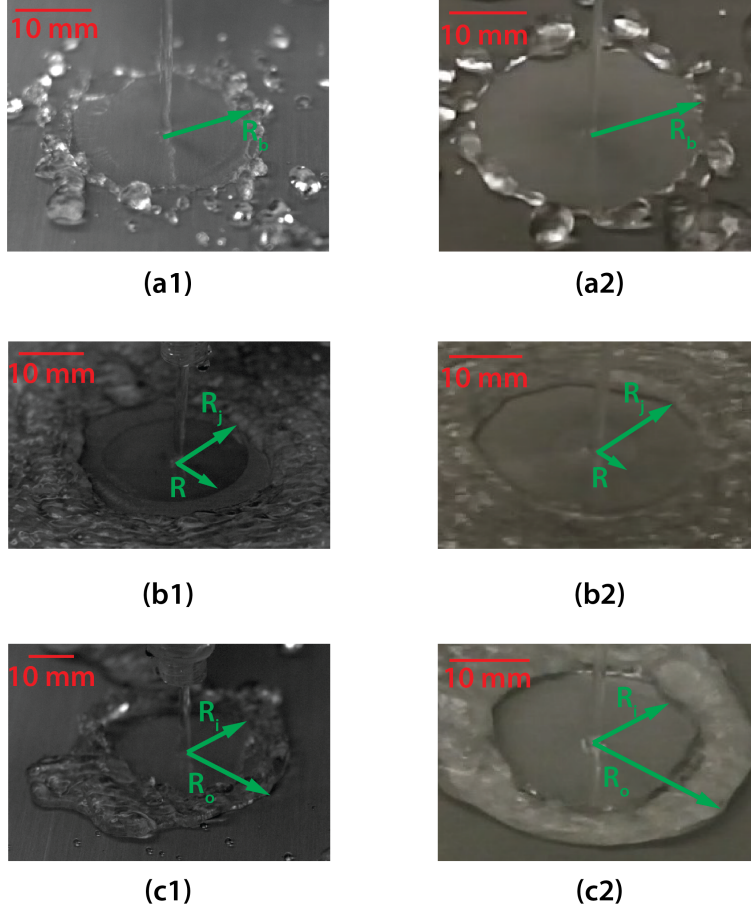
S1   Experiments at different flow rates

Figure S1: Snapshots of jet impingement events: on a design A-patterned substrate (Fig. 3ai of the main manuscript) (a1) at 800 mL/min with $R_b \simeq 19$ mm and (a2) at 1000 mL/min with $R_b \simeq 22$ mm; on a design B-patterned substrate (Fig. 3bi of the main manuscript) (b1) at 800 mL/min with $R = 16$ mm and $R_j \simeq 18$ mm and (b2) at 1000 mL/min with $R = 7$ mm and $R_j \simeq 21$ mm; on a design C-patterned susbtrate (Fig. 3ci of the main manuscript) (c1) at 800 mL/min with $R_i = 16$ mm and $R_o = 22$ mm and (c2) at 1000 mL/min with $R_i = 19$ mm and $R_o = 25$ mm.

Jet impingement events on substrates with wettability patterns A, B, and C (Fig. 3 of the main manuscript), and at two different flow rates (800 mL/min and 1000 mL/min), are shown in Fig. S1. Breakup (for design A) is seen at a radius $\simeq 22$ mm for the 1000 mL/min case, as compared to $\simeq 19$ mm for the 800 mL/min, while the hydraulic jump radii (for design B) are $\simeq 21$ mm and 18 mm for the two cases, respectively.

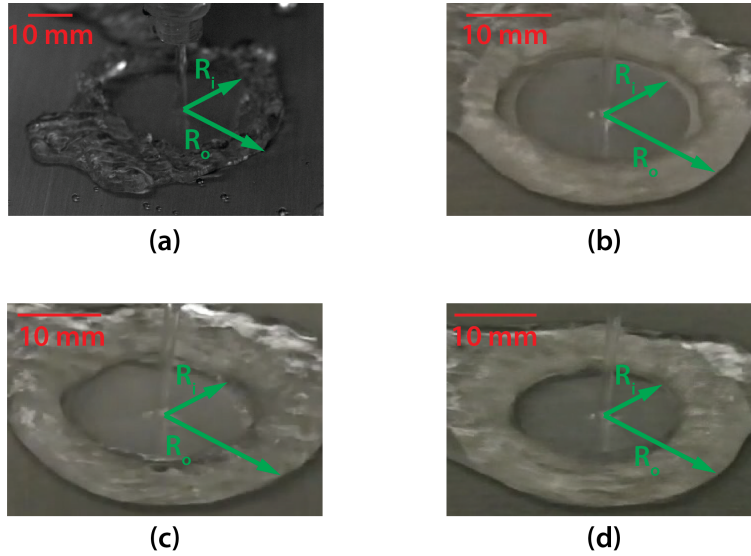# S2   Experiments for different pattern dimensions

Figure S2: Snapshots of jet impingement events on a design C-patterned substrate (Fig. 3ci of the main manuscript) at 800 mL/min with (a) $R_i = 16$ mm and $R_o = 22$ mm, (b) $R_i = 14$ mm and $R_o = 22$ mm, (c) $R_i = 16$ mm and $R_o = 24$ mm, and (d) $R_i = 14$ mm and $R_o = 24$ mm.

Jet impingement events, at 800 mL/min, on design C-patterned substrates (Fig. 3ci of the main manuscript) with different values of R_i and R_o are shown in Fig. S2. As expected, with increasing superhydrophilic area, the amount of liquid accumulation on the annulus increases.
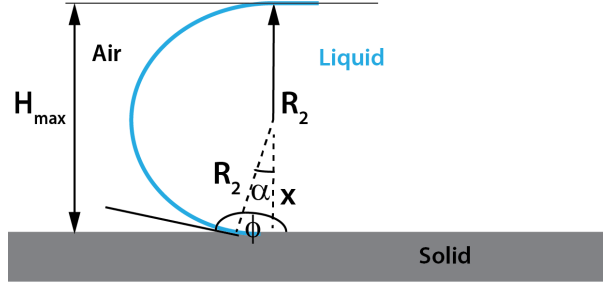
S3 Liquid height on a superhydrophobic surface

Figure S3: Schematic of the spreading liquid front on a superhydrophobic surface under jet impingement condition (inset of Fig. 4b of the main manuscript).

A schematic of the spreading liquid front, of radius R_2 and contact angle ϕ, under jet impingement condition on a superhydrophobic surface is shown in Fig. S3. The schematic represents the same situation as the one described in Fig. 4b of the main manuscript. The liquid jet, after impingement, spreads as a thin film on the superhydrophobic substrate, with the liquid film exhibiting a circular front (as shown in Fig. S3) prior to breaking up into droplets. From geometry,

$$x = R_2 \cos \alpha = R_2 \cos(\pi - \phi) \tag{1}$$

Hence, the maximum height of the film, H_{max}, is expressed geometrically as

$$H_{max} = R_2 + x = R_2[1 + \cos(\pi - \phi)] \tag{2}$$

and the corresponding hydrostatic pressure is given by $\rho g H_{max}$, where ρ is the density of the liquid. For a curved liquid interface, the pressure jump associated with the curvature is given by Laplace's equation

$$\Delta P = \sigma \left(\frac{1}{R_1} + \frac{1}{R_2} \right) \tag{3}$$

where R_1 and R_2 are the two radii of curvature at the surface. As mentioned in the main manuscript, $R_1 = R_b$, the radial location of film breakup, where $R_1 \gg R_2$. Hence,

$$\Delta P \simeq \frac{\sigma}{H_{max}}[1 + \cos(\pi - \phi)] \tag{4}$$

Equating the expressions for the Laplace pressure, ΔP, and the hydrostatic pressure (which is the condition for the maximum height), we obtain

$$\rho g H_{max}^2 = \sigma[1 + \cos(\pi - \phi)] \tag{5}$$

S4 Jet impingement at 600 mL/min and 1000 mL/min on design C-patterned substrate
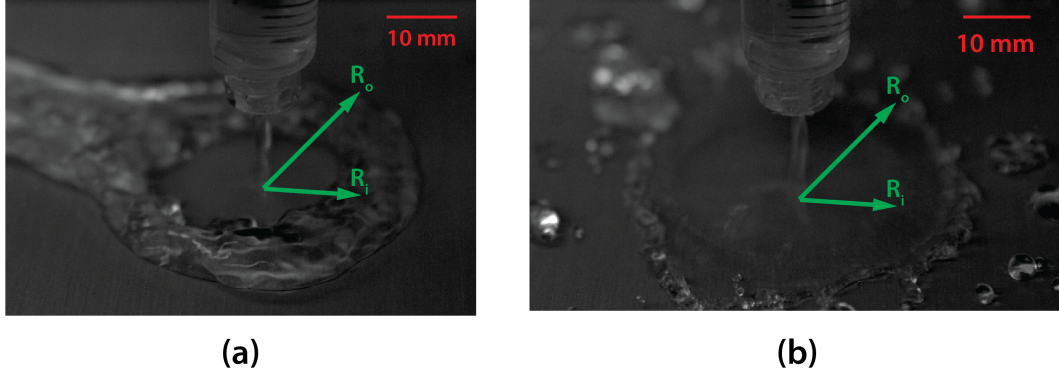

(a)   **(b)**

Figure S4: Snapshots of jet impingement events on a design C-patterned substrate (Fig. 3ci of the main manuscript), with $R_i = 16$ mm and $R_o = 22$ mm, for jet flow rate of (a) 600 mL/min and (b) 1000 mL/min.

Jet impingement events on the design C-patterned substrate (Fig. 3ci of the main manuscript), with $R_i = 16$ mm and $R_o = 22$ mm, at flow rates of 600 mL/min and 1000 mL/min are shown in Figs. S4a and S4b, respectively. These particular dimensions of the pattern are suitable for a flow rate of 800 mL/min, as evident from Fig. 3cii of the main manuscript. At the lower flow rate of 600 mL/min (Fig. S4a), the film breakup occurs at a radial location less than R_i. This was also concluded by studying the radial variation of the momentum force (per unit length) in Fig. 5 of the main manuscript. The film breakup is not distinct in Fig. S4a, since the film has much lower momentum (than that in the case of the 800 mL/min jet). Hence, after the film breakup, the droplets accumulate on the superhydrophilic annulus and form a pool of fluid. For the higher flow rate of 1000 mL/min (Fig. S4b), the film breaks up at a radial location ($\simeq 23$ mm) larger than R_o, which was also observed from the radial variation of momentum force (per unit length) in Fig. 5 of the main manuscript.
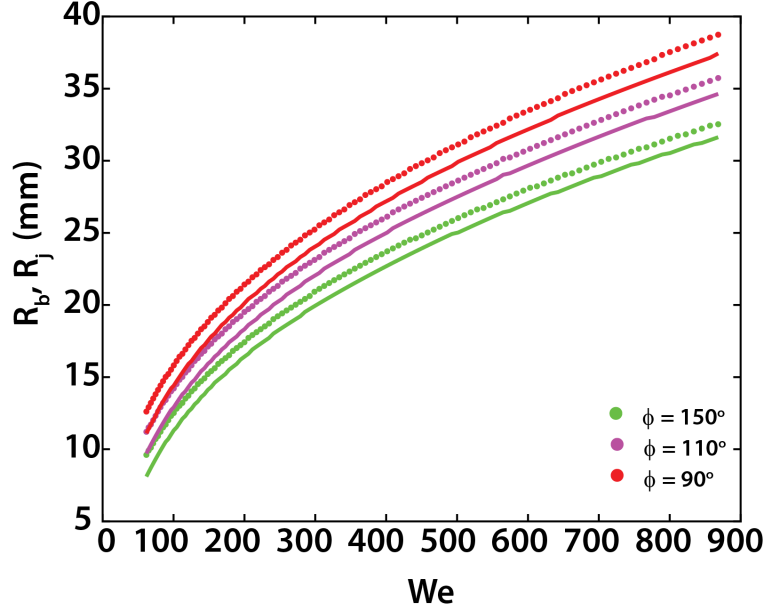
S5 Variations of R_b and R_j with We

Figure S5: Variations of R_b and R_j with We for three different values of ϕ (90°, 110°, and 150°); ϕ denotes the contact angle on the non-wettable domain. Each color represents one specific value of ϕ (see legend), and for each particular color, the solid line represents the variation of R_j, with the dotted line showing the variation of R_b.

The variations of R_b and R_j with We for three different ϕ values (90°, 110°, and 150°) are shown in Fig. S5. The plot is obtained from the theoretical model (Eqs. 7 and 10) described in the main manuscript. Each color is representative of one particular value of ϕ, and for each ϕ, the solid line represents the variation of R_j, while the dotted line shows the variation of R_b. Both R_b and R_j rise with We, with the rate of increase being faster at lower We values, as compared to higher We values. For a particular value of ϕ, the difference between R_b and R_j remains almost constant.

S6   Variations of capillary, gravity, and downstream depth terms with We
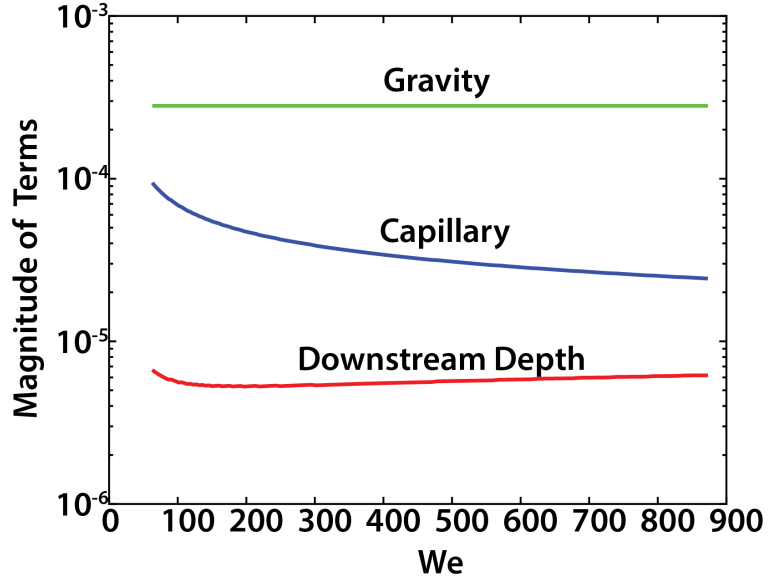

Figure S6: Variations of capillary, gravity, and downstream depth terms (terms in the left-hand side of Eq. 10 of the main manuscript) with We.

The variations of the capillary, gravity, and downstream depth terms (terms in the left-hand side of Eq. 10 of the main manuscript) with We are shown in Fig. S6. The equation is reproduced below for clarity. The first term on the left-hand side is for gravity, the second term is the capillary force, while the third term accounts for the downstream depth.

$$\frac{35}{17}\left(\frac{g(H^2 - h_j^2)}{2} + \frac{\sigma(H - h_j)}{\rho R_j} + \frac{a^4 V^2}{4R_j^2 H}\right) = U^2 h_j$$

S7   Non-dimensional forms of the governing equations

The governing equations presented in the main manuscript are reproduced in this section in their non-dimensional form. The dimensionless quantities are represented with a ' ^ 'over their symbols. All velocities are normalized by the jet velocity, V, while all lengths are normalized by the jet radius, a. The balance between gravity and surface tension can be expressed as

$$Bo\hat{H}_{max}^2 = \sigma[1 + \cos(\pi - \phi)] \tag{6}$$

where Bo denotes the Bond number, given by $Bo = \rho g a^2/\sigma$. The velocity profile in region 1 is given by

$$\hat{u} = \frac{3}{2}\frac{\hat{z}}{\hat{\delta}} - \frac{1}{2}\frac{\hat{z}^3}{\hat{\delta}^3} \tag{7}$$

while that in region 2 is expressed as

$$\hat{u} = \frac{3}{2}\hat{U}\frac{\hat{z}}{\hat{h}} - \frac{1}{2}\hat{U}\frac{\hat{z}^3}{\hat{h}^3} \tag{8}$$

where the radial variation of $\hat{U}$ is given by

$$\hat{U} = \frac{4}{5}\frac{1}{\hat{r}\hat{h}} \tag{9}$$

The pressure jump across the edge of the spreading film front can be expressed as

$$\frac{\Delta P a}{\sigma} = \frac{1}{\hat{h}}[1 + \cos(\pi - \phi)] \tag{10}$$

The condition for breakup in region 1 can be expressed as

$$\frac{1}{We}[1 + \cos(\pi - \phi)] = (\hat{h} - \frac{18}{35}\hat{\delta}) \tag{11}$$

while that in region 2 is given by

$$\frac{1}{We}[1 + \cos(\pi - \phi)] = \frac{17}{35}\hat{U}^2\hat{h} \tag{12}$$

The equilibrium at the hydraulic jump yields

$$Bo\frac{\hat{H}^2 - \hat{h}_j^2}{2} + \frac{\hat{H} - \hat{h}_j}{\hat{R}_j} + \frac{We}{4\hat{R}_j^2\hat{H}} = \frac{17}{35}We\hat{U}^2\hat{h}_j \tag{13}$$

and the post-jump velocity is given by

$$\hat{U}_2 = \left(\frac{17}{35}\frac{\hat{h}_j}{\hat{H}_{max}} - \frac{1}{2}\frac{ga}{V^2}\frac{\hat{H}_{max}^2 - \hat{h}_j^2}{\hat{H}_{max}} - \frac{1}{We}\frac{\hat{H}_{max} - \hat{h}_j}{\hat{H}_{max}\hat{R}_j}\right)^{1/2} \tag{14}$$